Phase variation of ferroelectric math xmlns="http://www.w3.org/1998/Math/MathML">mrow>msub>mi>Li/mi>mn>2/mn>/msub>msub>mi>Sr/mi>mrow>mn>1/mn>mo>−/mo>mi>x/mi>/mrow>/msub>msub>mi>Ca/mi>mi>x/mi>/msub>msub>mrow>mo>(/mo>mrow>msub>mi>Nb/mi>mrow>mn>1/mn>mo>−/mo>mi>x/mi>/mrow>/msub>msub>mi>Ta/mi>mi>x/mi>/msub>/mrow>mo>)/mo>/mrow>mn>2/mn>/msub>msub>mi mathvariant="normal">O/mi>mn>7/mn>/msub>/mrow>/math> by selective reinforcement in the (Nb,Ta)-O covalent bonds

Akitoshi Nakano, Hirokazu Shirakuni, Takayuki Nagai, Yasuhide Mochizuki, Fumiyasu Oba, Hiroko Yokota, Shogo Kawaguchi, Ichiro Terasaki, and Hiroki Taniguchi

Phys. Rev. Materials **6**, 044412 — Published 25 April 2022

DOI: 10.1103/PhysRevMaterials.6.044412

Phase variation of ferroelectric $Li_2Sr_{1-x}Ca_x(Nb_{1-x}Ta_x)_2O_7$ by selective reinforcement in the (Nb,Ta)-O covalent bonds

Akitoshi Nakano[1*], Hirokazu Shirakuni[1], Takayuki Nagai[1],
Yasuhide Mochizuki[2], Fumiyasu Oba[2], Hiroko Yokota[3], Shogo Kawaguchi[4],
Ichiro Terasaki[1], and Hiroki Taniguchi[1]

[1]*Department of Physics, Nagoya University, Nagoya 464-8602, Japan*
[2]*Laboratory for Materials and Structures, Institute of Innovative Research, Tokyo Institute of Technology, Yokohama 226-8503, Japan*
[3] *Department of Physics, Faculty of Science and Engineering, Chiba University, 1-33 Yayoi-cho, Inage-ku, Chiba 263-8522, Japan*
[4]*Japan Synchrotron Radiation Research Institute (JASRI), SPring-8, Hyogo 679-5198, Japan*

A phase variation of a pseudo Roddlesden-Popper-type ferroelectric oxide $Li_2Sr_{1-x}Ca_x(Nb_{1-x}Ta_x)O_7$ is systematically investigated using dielectric measurements, second harmonic generation, and x-ray diffraction experiments. We find an exotic *x*-*T* phase diagram, including paraelectric *Cmcm*, antiferroelectric *Pmcn*, and in-plane antiferroelectric and out-of-plane ferroelectric $P2_1cn$ phases. At low *x*, we observe large and divergent dielectric anomalies associated with phase transitions from *Cmcm* to $P2_1cn$, whereas these become small kinks at high *x*. Structural analyses reveal an internal distortion, and the rotation of octahedra strongly depends on *x*, which is consistent with the lattice dynamics obtained by a density functional theory calculation. These results demonstrate the great tunability of dielectric properties in layered perovskite-type oxides by tuning the chemical bonding state in the octahedron.

I. INTRODUCTION

Ferroelectricity is one of the most intriguing emergent phenomena in condensed matter physics. Perovskite-type oxides, with a chemical formula of the form ABO_3, are some of the most typical ferroelectric materials. The microscopic mechanism of the perovskite-type ferroelectric oxides has been understood as the second-order Jahn-Teller (SOJT) effect, in which the covalency between the *A* or *B* cation and oxygen ions plays a vital role in inducing spontaneous polarization [1]-[13]. In contrast to this "proper" ferroelectricity which comes from an electronic origin, the hybrid "improper" ferroelectricity (HIF) [14][15], the mechanism of which has been understood as the geometrical instabilities of the octahedra network, has recently been proposed in layered perovskite-type oxides. Especially, the Ruddlesden-Popper (RP)-type layered oxides, having a chemical formula of the form $A_3B_2O_7$, have been extensively studied as an ideal platform for HIF [16]-[20]. Since these two distinct types of ferroelectricity have been developed in the different platforms, the system in which both instabilities compete or cooperative has hardly been investigated. We can expect some exotic dielectric properties in such system.

In this context, a unique ferroelectricity has been reported in an *A*-site ordered "pseudo" RP (pRP)-type oxide $Li_2SrNb_2O_7$ (LSNO) [21][22]. This compound shows a divergent growth of the dielectric permittivity, which is reminiscent of proper ferroelectricity, around 210 K [21][22]. This is different from ordinary RP-type oxides which show tiny dielectric anomalies associated with the hybrid improper ferroelectric phase transitions [23]. Thus, it is indicated that the SOJT instability plays a vital role in LSNO instead of the geometrical instabilities. Furthermore, LSNO shows a double hysteresis like polarization-electric field (*P* - *E*) curve below 100 K, indicating its complex dielectric nature [21][22].

More interestingly, $Li_2CaTa_2O_7$ (LCTO) [24], another isostructural pRP-type compound, shows distinct dielectric properties from LSNO. LCTO shows a tiny dielectric anomaly associated with the phase transition and exhibits a standard ferroelectric *P*-*E* curve [25]. These features are reminiscent of the HIF [16]-[20]. The qualitative difference in dielectric properties between isostructural LSNO and LCTO indicates the inhered instability possibly differs between these two systems. The understanding how the microscopic mechanism changes in the isostructural system can provide a new insight to the field of ferroelectricity.

In this article, we systematically conducted dielectric measurements and structural analyses on solid solutions $Li_2Sr_{1-x}Ca_x(Nb_{1-x}Ta_x)_2O_7$ (LSCNTO-*x*). We find that the complete solid solution can be formed in this system, and LSCNTO-*x* has a unique phase

diagram including paraelectric, antiferroelectric and ferroelectric phases. We demonstrate that the inhered SOJT and geometrical instability continuously change upon varying x. The changing in the atomic orbital component in B - O covalent bonding may be a possible route to tune the dielectric responses of the layered perovskite-type oxides.

II. METHODS

The polycrystalline samples of LSCNTO-x for x = 0, 0.1, 0.2, 0.3, 0.4, 0.5 and 0.6 were prepared by a conventional solid-state reaction method with powder mixtures of Li_2CO_3 (99.9 %), $SrCO_3$ (99.9%), $CaCO_3$ (99.9%), Ta_2O_5(99.99%) and Nb_2O_5 (99.99%), where excess Li_2CO_3 (10% mol) was added to compensate the volatility of Li_2O at high temperatures [21]. For x = 0.7, 0.8, 0.9 and 1, the products prepared by the method above included large amount of impurity phases and showed poor crystallinity due to the short-time and low-temperature sintering condition. Thus, we sintered the pelletized products at 1150 □ three times while adding some amount of Li_2CO_3 each time. After that, we loaded the products wrapped by Pt sheets into evacuated tubes and baked them for 6 hours. We characterized the obtained powder by x-ray diffraction (XRD) measurements with a wavelength of 0.77 □ using a BL02B2 [26] beamline at SPring-8. The profile-fitting analyses were conducted using Jana2006 [27]. Since samples of x = 0 ~ 0.4, 0.6, and 1 were strongly influenced by the stacking fault and preferred orientation effects, we calculated the lattice parameters for all LSCNTO-x by the LeBail method. We successfully conducted the Rietveld refinement at 100 K for x = 0.5, 0.7, 0.8, and 0.9 specimens. We also picked a single crystal for x = 0 from the polycrystalline sample and characterized it using BL02B1 [28] beamlines at SPring-8. The crystal-structure analysis was performed by means of a least squares program, SHELXL [29]. Dielectric permittivity was measured by using a 4284A precision LCR meter. The second harmonic generation was measured by a reflection mode using an Nd:YVO_4 laser with a wavelength of 1064 nm and a repetition frequency of 2.5 kHz. First-principles calculations used the projector augmented-wave method [30] and the PBEsol functional [31] within the generalized gradient approximation as implemented in VASP [32][33]. The phonon bands were calculated with 2 × 2 × 2 supercells that were constructed from the expansion of the primitive cells using force constants derived from PHONOPY [34]. Furthermore, to explore the dynamically stable structure, we set a $\sqrt{2} \times \sqrt{2} \times 1$ supercell of the conventional *I*4/*mmm* phase so that the zone-boundary special points X (1/2, 1/2, 0) and M (0, 0, 1) are folded into the Γ point. Note that the *I*4/*mmm* phase possesses

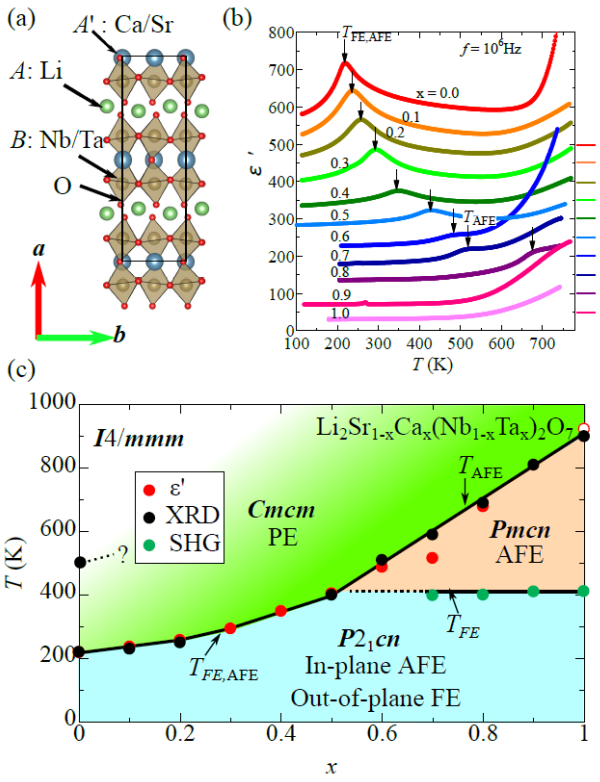

FIG. 1. (a) Crystal structure of $Li_2Sr_{1-x}Ca_x(Nb_{1-x}Ta_x)_2O_7$ viewed from the c-axis. The structure is visualized using VESTA [43] (b) Temperature dependence of the dielectric permittivity on various x. The zero points of the curves are each shifted in increments of 50 for visibility and are indicated by the color lines by the side of the graph. (c) The phase diagram of $Li_2Sr_{1-x}Ca_x(Nb_{1-x}Ta_x)_2O_7$. The abbreviations of PE, AFE, and FE denote paraelectricity, antiferroelectricity, and ferroelectricity, respectively. The open circle data for x = 1 is referred to ref. [25].

no distortion. Through calculating the phonon band of the supercell, we can derive imaginary phonon modes at X and M points of *I*4/*mmm* in Γ point at once, the method of which was used in the previous studies [36]-[40]. The calculation of the phonon band is performed until no imaginary phonon mode appears. The chemical bonding analysis through crystal orbital Hamiltonian populations (COHPs) was performed using LOBSTER [41][42].

III. RESULTS & DISCUSSION

Here, we take a closer look at the crystal structure of the n = 2 pseudo pRP-type compounds that have a chemical formula of the form $A_2A'B_2O_7$. In the n = 2 pRP-type structure, single distorted rock salt A_2O and double perovskite-type $A'B_2O_6$ blocks stack in order along the a-axis direction. In LSCNTO-x, Li, Sr (Ca),

and Nb (Ta) occupy the *A*, *A'*, and *B* sites, respectively, as shown in Fig. 1(a). Compared to ordinary $n = 2$ RP-type phases, such as $Sr_3Zr_2O_7$, $Ca_3Ti_2O_7$, etc., the interlayer distance between perovskite blocks is shorter by 20% in LSCNTO-*x* because of such distorted Li-O blocks.

We observe a systematic change in the dielectric responses of LSCNTO-*x*, as shown in Fig. 1(b). LSNO ($x = 0$) shows a diverged dielectric permittivity on the verge of the phase transition around 217 K. This trend is consistent with previous results [21][22]. When we increase *x*, the peak temperature shifts higher and the anomaly gradually weakens. This behavior is also consistent with the previous result, where a small anomaly was observed in the paraelectric-to-antiferroelectric phase transition in LCTO ($x = 1$) [25], suggesting a change in the dielectric nature upon chemical substitution.

We summarized the phase diagram of LSCNTO-*x* in Fig. 1(c). Note that the phase diagram is determined by not only the dielectric measurements but also by the temperature dependent lattice constants and the SHG measurements [44]. In this paper, we focus on three phases in the *x*-*T* diagram: the paraelectric *Cmcm* phase, the antiferroelectric *Pmcn* phase, and the in-plane antiferroelectric and out-of-plane ferroelectric $P2_1cn$ phase. Note that a phase boundary between proto-type *I*4/*mmm* and *Cmcm* [22] has not been determined yet, although we have confirmed that *Cmcm* phase continues up to 970 K at $x = 0.5$ [45]. The successive transition from *Cmcm* to $P2_1cn$ via *Pmcn* is consistent with the previous report on LCTO [47]. We define the transition temperatures from *Cmcm* to *Pmcn* and from *Pmcn* to $P2_1cn$ as T_{AFE} and T_{FE}, respectively. We should note that the phase boundaries of the successive phase transitions seem to merge between $x = 0.5$ and 0.6, and we infer the ferroelectric-antiferroelectric-paraelectric triple point similar to perovskite-type ferroelectric materials [48] exists in the *x* -*T* diagram. At $x < 0.5$. the paraelectric *Cmcm* phase directly turns to in-plane antiferroelectric and out-of-plane ferroelectric $P2_1cn$ phase. Thus, we define this transition temperature as $T_{FE,AFE}$.

Here, we should note that the phase assignment for $x = 0$ is different from ref 22. In ref 22., Uppuluri et al. have argued that an in-plane polar $A2_1am$ ($Cmc2_1$ in our setting) phase realizes at room temperature and an in-plane anti-polar *Pnam* (*Pmcn*) phase realizes at lower temperatures [22]. In addition, the coexistence of $A2_1am$ and *Pnam* phases was observed between 100 K and 250 K [22]. On the other hand, we have previously proposed that a paraelectric *Cmcm* phase realizes at room temperature and it changes to an in-plane antiferroelectric and out-of-plane ferroelectric $P2_1cn$ phase below 217 K [21]. The low-temperature ferroelectricity has been confirmed by a small spontaneous polarization in *P*-*E* curve [21]. We should also note that the coexistence of phases has not been observed in our powder XRD [46]. In this paper, we have done the phase assignment based on our previous result. The phase boundaries naturally connect between $x = 0$ and 1 based on our phase assignment for $x = 0$.

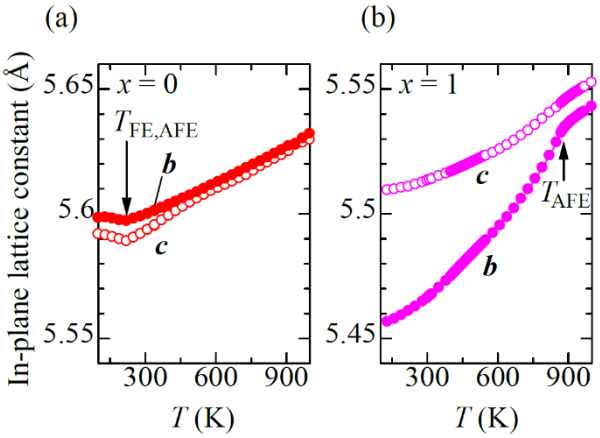

FIG. 2. Temperature dependence of the in-plane lattice constants (*b* and *c*) for (a) $x = 0$ and (b) $x = 1$ by the LeBail fitting. In each figure, filled and open circles show the *b*- and *c*-axes, respectively.

The *x*-*T* phase diagram for LSCNTO-*x* is unique in the following points: (i) The co-substitution effect is weak at low *x* (< 0.4), where $T_{FE,AFE}$ slowly increases with the slope of $dT_{FE,AFE}/dx = 1.5$ K/%. (ii) T_{AFE} rapidly increases with the slope of $dT_{AFE}/dx = 10$ K/% at high *x* (> 0.5). These features are not similar to those of the single-substituted system, $Li_2Sr(Nb_{1-x}Ta_x)_2O_7$ and $Li_2Sr_{1-x}Ca_xNb_2O_7$. In the case of $Li_2Sr(Nb_{1-x}Ta_x)_2O_7$, $T_{FE,AFE}$ *decreases* with a linear slope of 6 K/% and completely vanishes at $x = 0.4$ [49]. In the case of $Li_2Sr_{1-x}Ca_xNb_2O_7$, $T_{FE,AFE}$ *increases* with a slope of 6 K/% until $x = 0.2$ [36]. According to the single-substitution effects, we infer that the slow increase of $T_{FE,AFE}$ at low *x* (< 0.4) stems from the competition between the single Ca- and Ta-substitution effects. However, the rapid increase in T_{AFE} at high *x* (> 0.5) cannot be explained as a competitive picture of individual single-substitution effects similar to low *x* (< 0.4).

The temperature dependence of the in-plane lattice constants (*b*- and *c*-axes) clearly unveils the qualitative difference between low- and high-*x* systems. Figure 2(a) and 2(b) shows the temperature dependence of the in-plane lattice constants for the $x = 0$ and $x = 1$ samples, respectively, obtained by the LeBail fitting assuming the *Pmcn* space group at all temperatures. For $x = 0$, the in-plane lattice constants *b* and *c* correspond within 0.05% between 500 K and 1000 K, indicating that the higher symmetry *I*4/*mmm* phase exists above 500 K as previously reported [22]. Below 500 K, the in-plane

lattice constants begin to show anisotropy due to out-of-plane tilt of the BO_6 octahedra. Most notably, the in-plane lattice constants increase as temperature decreases below $T_{FE,AFE} \approx 220$ K. This in-plane negative thermal expansion is similar to that just below the cubic-tetragonal phase transitions of the perovskite-type ferroelectric materials, where the shape of BO_6 octahedra become distorted by the strong SOJT effect [50]. We also note that the anisotropy of the in-plane lattice constants $||\boldsymbol{c}|/|\boldsymbol{b}|-1|$ hardly changes between 220 K (0.14 %) and 100 K (0.12 %).

In contrast, for $x = 1$, the in-plane lattice constants decrease below $T_{AFE} \approx 900$ K, and the in-plane anisotropy is enhanced from 900 K (0.17 %) to 100 K (0.90 %). Such anisotropic shrink of cell parameters has been frequently observed in HIF layered perovskite-type oxides [20], where BO_6 octahedra rotate perpendicularly to the interlayer axis. In addition, we have not observed the phase transition from *Cmcm* to *I*4/*mmm* for $x = 1$ until 1000 K. The temperature dependence of the lattice constants for other-x is summarized in Fig. S1 [44].

To elucidate the origin of the unusual phase diagram, we investigate the x-dependence of the crystal structure of LSCNTO-x at 100 K. Here, we focus on two distinct structural features: (i) the displacement of the B-cation along the c-axis, which deforms the BO_6 octahedron as shown in Fig. 3(a), and (ii) the in-plane lattice anisotropy induced by the rotation of BO_6 octahedra around the a-axis, as shown in Fig. 3(b). We can consider that (i) is a measure for the SOJT instability and (ii) is a measure for geometrical instability.

Figure 3(c) shows the x-dependence of δl, which is a product of the c-axis length and change in the fractional coordinate of B-cation from *Cmcm* phase, at 100 K. Note that we obtained δl by assuming the *Pmcn* structure to reduce the refinable parameters, although the actual space group of LSCNTO-x at 100 K is $P2_1cn$ [51].δl reaches almost 0.1 □ for $x = 0$, when we use the parameters $c = 5.5982$ □ and the change in the fractional coordinate of 0.01696 (see Tables S1 [52] and S2 of ref. [21]). This value is comparable to that of Ti ions in $BaTiO_3$, which is associated with the cubic-to-tetragonal transition. On the other hand, the in-plane lattice anisotropy $||\boldsymbol{c}|/|\boldsymbol{b}|-1|$ in Fig. 3 (c) is very small due to the small rotation of NbO_6 octahedra. This indicates that the SOJT instability dominates the phase transition in early LSCNTO-x. δl decreases upon increasing x, indicating the weakening of the SOJT instability. Instead, the in-plane lattice anisotropy rapidly increases above $x = 0.4$, indicating the enhancement of the rotation of the BO_6 octahedra induced by the geometrical instability.

Interestingly, the small but finite δl exists at $x = 0.7$, 0.8, 0.9, and 1 [47]. This is in contrast to the result of $Li_2Sr(Nb_{1-x}Ta_x)_2O_7$, where δl vanishes at $x = 0.4$ as a result of the complete disappearance of the SOJT

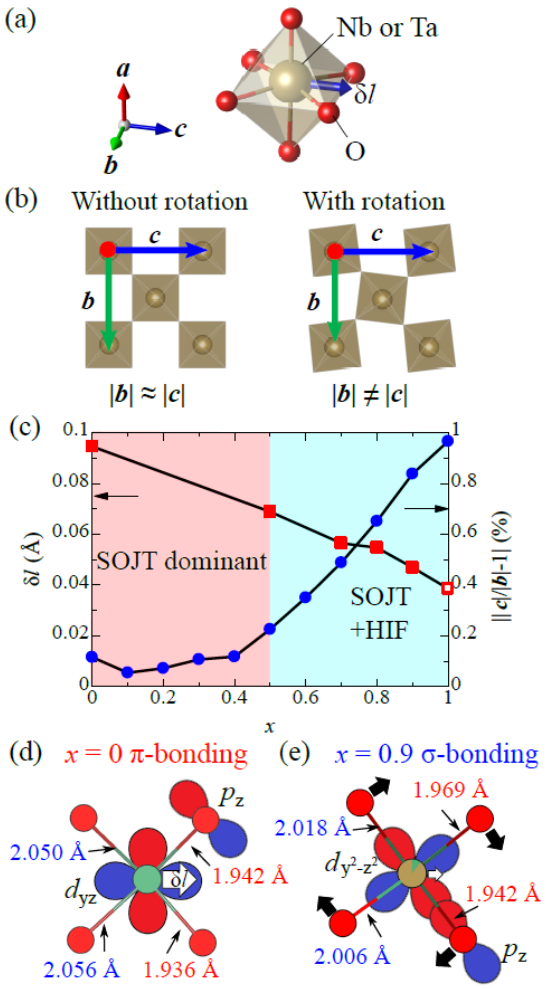

FIG. 3. Schematics of (a) the displacement of B-cation in an octahedron, (b) the in-plane lattice anisotropy induced by the octahedra rotation. The blue vector in (a) shows the B-cation displacement along the c-axis (δl). (c) The x-dependence of δl and lattice anisotropy at 100 K. The open square data for $x = 1$ is evaluated from RT data of Table 1 and 2 in ref. [24] (the two Ta-site are averaged). Schematics of the (d) π-bonding and (e) σ-bonding in a BO_6 octahedron. The analyzed bond lengths between B-cation and oxygens are also shown for $x = 0$ and $x = 0.9$.

instability [49]. This indicates that, when we vary x of LSCNTO-x above 0.4, there is not a simple crossover of the transition mechanism from the SOJT to geometrical instability. As described below, the SOJT effect survives in the strongly rotated BO_6 octahedra with the change in the chemical bonding nature at high x compositions.

Figures 3(d) and 3(e) schematically shows the analytical in-plane bond lengths of the BO_6 octahedra for $x = 0$ and $x = 0.9$, respectively. For $x = 0$, δl is large, whereas the rotation is very small, resulting in an almost isotropic decrease in two Nb-O bonds by 5%.

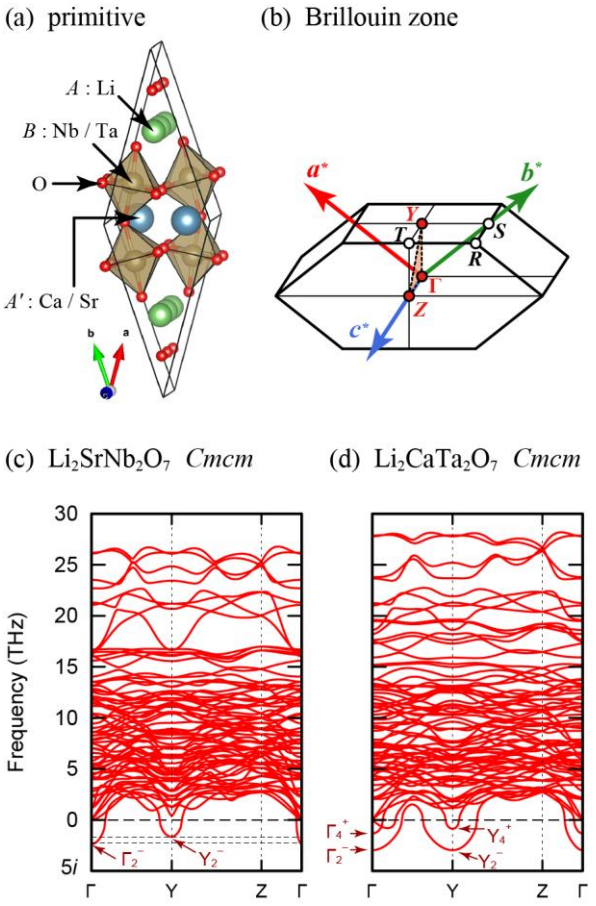

FIG. 4. (a) Primitive cell of the *Cmcm* phase for $Li_2A'B_2O_7$, which is derived from the first-principles calculations. The structure is visualized with VESTA [43]. (b) The Brillouin zone of based-centered-orthorhombic Bravais lattice, which includes the space group *Cmcm* [55]. The red, green, and blue axes respectively indicate the reciprocal lattice vectors a^*, b^*, and c^* in the *Cmcm* primitive cell. The broken line shows the band path used in the phonon band calculation. Calculated phonon band structures of (c) $Li_2SrNb_2O_7$ [36][49] and (d) $Li_2CaTa_2O_7$ in the paraelectric *Cmcm* phases. Frequencies less than zero have imaginary units. Irreducible representations with imaginary frequency are also indicated.

This trend is understood by means of the enhanced covalency of the π-bonding orbital, which consists of Nb-4d_{yz} and O-2p_z orbitals as shown in Figs. 3(d) and S6(e) [49][52]. On the other hand, for x = 0.9, the combination of the SOJT and geometrical instability leads to an anisotropic decrease in *B*-O bonds; the difference between the shortest and longest is about 4% and that between the second shortest and longest is about 2%, which are consistent with the calculation results [54]. This situation has been recently predicted in $Li_2CaNb_2O_7$ [36], where the σ-bonding, which consists of Nb-4d_{y2-z2} and O-2p_z, is reinforced to give rise to a global energy lowering as shown in Fig. 3(e). Such trend is also confirmed for LCTO by the crystal orbital Hamiltonian population analysis (Fig. S6 [52]).

We infer the bonding orbital, which drives the phase transition, switches from π- to σ- bonding above $x = 0.4$, since the lattice anisotropy $||\boldsymbol{c}|/|\boldsymbol{b}|-1|$ starts to increase at that x. The rapid increase of dT_{AFE}/dT at high x (> 0.5) must be related to this switching. We also deduce that the switching of the bonding nature gives rise to the emergence of the antiferroelectric phase above $x = 0.5$.

Let us discuss the phase transitions in LSNO and LCTO from the viewpoint of the lattice dynamics. Figure 4 (a) and 4 (b) show the primitive cell and Brillouin zone of the *Cmcm* phase. In this setting, the zone-boundary special points of *Y* and *Z* are defined respectively as (1/2, 1/2, 0) and (0, 0, 1/2), which can be represented as 1/2 $\boldsymbol{a}^*$ + 1/2 $\boldsymbol{b}^*$ and 1/2 $\boldsymbol{c}^*$ [52]. The band dispersions, which are shown in Fig. 4 (c) and 4 (d), are calculated along the path of Γ-Y-Z-Γ.

For LSNO (Fig. 4(c)), an imaginary Γ_2^- mode is the most unstable. This indicates a potential soft phonon mode at Γ point which results in a proper ferroelectricity [56]-[58]. Although, the freezing of the Y_2^- mode has been experimentally confirmed in LSNO [21], the divergent growth of the dielectric permittivity around $T_{FE,AFE}$ at low x (< 0.4) may stem from the softening of Γ mode. On the other hand, for LCTO (Fig. 4 (d)), the imaginary frequency of the zone-boundary Y_2^- mode becomes as large as that of the Γ_2^- mode. The weakening of the dielectric anomalies around T_{AFE} at high x (> 0.5) may come from the hardening of the Γ_2^- soft mode relative to the Y_2^- mode. Since the direction of Γ–Y corresponds to the *a*+*b* direction in the primitive cell (*a*-axis direction of the conventional cell), the Y_2^- soft mode can generate the anti-parallel displacement of *B*-cation and *out-of-phase* octahedral rotations between stacking double-perovskite layers. Actually, theoretically derived stable structures by freezing Y_2^- modes of LSNO and LCTO strongly support our structural analyses; the displacement of Nb in LSNO is larger than Ta in LCTO, whereas the rotation of NbO_6 octahedron in LSNO is much smaller than TaO_6 octahedron in LCTO [54].

Our present result clearly shows that LSCNTO-*x* is a very useful playground to control the ferroelectricity through tuning two-types of the instabilities in the identical crystal structure. Such dual tunability has not been taken into account in the typical perovskite-type and RP-type oxides thus far. We infer that short interlayer distance and asymmetric crystal field of the BO_6 octahedra play a role to render the intermediate dielectric and phase transition properties between perovskite-type- and layered perovskite-type oxides to pRP phases.

IV. SUMMARY

In summary, we revealed an intriguing $x - T$ phase diagram for $Li_2Sr_{1-x}Ca_x(Nb_{1-x}Ta_x)O_7$ (LSCNTO-x). At low x (< 0.4), the SOJT effect mainly drives the phase transition, whereas at high x (> 0.5), geometrical instability becomes effective. We have revealed that the steep enhancement of the transition temperature above x = 0.5 stems from the cooperative mechanism of the SOJT effect and geometrical instability. We propose that LSCNTO-x is a useful playground to investigate the relationship between structures, electronic states, and functionalities in layered perovskite ferroelectric materials.

ACKNOWLEDGEMENT

This work is partly supported by the Murata Science Promotion Foundation (Proposal No. H31-69). Single-crystal and powder XRD measurements were conducted with the approval of the Japan Synchrotron Radiation Research Institute (JASRI) (Proposal No. 2019B1332, 2020A1431, and 2020A1246). This work was partly supported by Nanotechnology Platform Program (Molecule and Material Synthesis) of the Ministry of Education, Culture, Sports, Science and Technology (MEXT), Japan, Grant Number JPMXP09S20NU0029.

[1] R. G. Pearson, A symmetry Rule for Predicting Molecular Structures, J. Am. Chem. Soc. 91, 4947 (1969)
[2] R. G. Pearson, The second-order Jahn-Teller effect, J. Mol. Struct.: THEOCHEM 103, 25 (1983)
[3] T. Hughbanks, Superdegenerate Electronic Energy Levels in Extended Structures, J. Am. Chem. Soc. 107, 6851 (1985)
[4] R. A. Wheeler, M. H. Whangbo, T. Hughbanks, R. Hoffmann, J. K. Burdett, T. A. Albright, Symmetric vs. asymmetric linear M-X-M linkages in molecules, polymers, and extended networks, J. Am. Chem. Soc. 108, 2222 (1986)
[5] R. E. Cohen, Origin of ferroelectricity in perovskite oxides, Nature, 358, 136 (1992)
[6] M. Posternak, R. Resta, A. Baldereschi, Role of covalent bonding in the polarization of perovskite oxides: The case of $KNbO_3$, Phys. Rev. B: Condens. Matter Mater. Phys. 50, 8911 (1994)
[7] M. Kunz, I. D. Brown, Out-of-Center Distortions around Octahedrally Coordinated d^0 Transition Metals, J. Solid State Chem. 115, 395 (1995)
[8] J. B. Goodenough, JAHN-TELLER PHENOMENA IN SOLIDS, Annu. Rev. Mater. Sci. 28, 1 (1998)
[9] Y. Kuroiwa, S. Aoyagi, A. Sawada, J. Harada, E. Nishibori, M. Takata, M. Sakata, Evidence for Pb-O Covalency in Tetragonal $PbTiO_3$, Phys. Rev. Lett. **87,** 217601 (2001)
[10] H. Taniguchi, H. P. Soon, T. Shimizu, H. Moriwake, Y. J. Shan, M. Itoh, Mechanism for suppression of ferroelectricity in $Cd_{1-x}Ca_xTiO_3$, Phys. Rev. B: Condens. Matter Mater. Phys. 84, 174106 (2011)
[11] H. Moriwake, A. Kuwabara, C. A. J. Fisher, H. Taniguchi, M. Itoh, I. Tanaka, First-principles calculations oflattice dynamics in $CdTiO_3$ and CaTiO3: Phase stability and ferroelectricity, Phys. Rev. B: Condens. Matter Mater. Phys. 84, 104114 (2011)
[12] H. Taniguchi, H. P. Soon, H. Moriwake, Y. J. Shan, M. Itoh, Effect of Ca-Substitution on CdTiO3 Studied by Raman Scattering and First Principles Calculations, Ferroelectrics 426, 268 (2012)
[13] I. B. Bersuker, Pseudo Jahn-Teller Origin of Perovskite Multiferroics, Magnetic-Ferroelectric Crossover, and Magnetoelectric Effects: The d0-d10 Problem, Phys. Rev. Lett. 108, 137202 (2012)
[14] N. A. Benedek, C. J. Fennie, Hybrid Improper Ferroelectricity: A Mechanism for Controllable Polarization-Magnetization Coupling, Phys. Rev. Lett. 106, 107204 (2011)
[15] N. A. Benedek, A. T. Mulder, C. J. Fennie, Polar octahedral rotations: A path to new multifunctional materials, J. Solid State Chem. 195, 11 (2012)
[16] Y. S. Oh, X. Luo, F.-T. Huang, Y. Wang, S.-W. Cheong, Experimental demonstration of hybrid improper ferroelectricity and the presence of abundant charged walls in $(Ca,Sr)_3Ti_2O_7$ crystals, Nat. Mater., 14, 407 (2015)
[17] X. Q. Liu, B. H. Chen, J. J. Lu, Z. Z. Hu, X. M. Chen, Hybrid improper ferroelectricity in B-site substituted $Ca_3Ti_2O_7$: The role of tolerance factor, Appl. Phys. Lett. 113, 242904 (2018)
[18] S. Yoshida, K. Fujita, H. Akamatsu, O. Hernandez, A. Sen Gupta, F. G. Brown, H. Padmanabhan, A. S. Gibbs, T. Kuge, R. Tsuji, S. Murai, J. M. Rondinelli, V. Gopalan, K. Tanaka, Ferroelectric $Sr_3Zr_2O_7$: Competition between Hybrid Improper Ferroelectric and Antiferroelectric Mechanisms, Adv. Funct. Mater. 28, 1801856 (2018)
[19] Y. Wang, F. T. Huang, X. Luo, B. Gao, S. W. Cheong, The First Room-Temperature Ferroelectric Sn Insulator and Its Polarization Switching Kinetics, Adv. Mater. 29, 1601288 (2017)
[20] S. Yoshida, H. Akamatsu, R. Tsuji, O. Hernandez, H. Padmanabhan, A. Sen Gupta, A. S. Gibbs, K. Mibu, S. Murai, J. M. Rondinelli, V. Gopalan, K. Tanaka, K. Fujita, Hybrid Improper Ferroelectricity in $(Sr,Ca)_3Sn_2O_7$ and Beyond: Universal Relationship between Ferroelectric Transition Temperature and Tolerance Factor in n = 2 Ruddlesden-Popper Phases, J. Am. Chem. Soc.

140, 15690 (2018)
[21] T. Nagai, H. Shirakuni, A. Nakano, H. Sawa, H. Moriwake, I. Terasaki, H. Taniguchi, Weak Ferroelectricity in n = 2 Pseudo Ruddlesden-Popper-Type Niobate $Li_2SrNb_2O_7$, Chem. Mater. 31, 6257 (2019)
[22] R. Uppuluri, H. Akamatsu, A. Sen Gupta, H. Wang, C. M. Brown, K. E. Agueda Lopez, N. Alem, V. Gopalan, T. E. Mallouk, Competing Polar and Antipolar Structures in the Ruddlesden?Popper Layered Perovskite $Li_2SrNb_2O_7$, Chem. Mater. 31, 4418 (2019)
[23] B. H. Chen, T. L. Sun, X. Q. Liu, X. L. Zhu, H. Tian, and X. M. Chen, Enhanced hybrid improper ferroelectricity in $Sr_{3-x}Ba_xSn_2O_7$ ceramics with a Ruddlesden-Popper (R-P) structure, Appl. Phys. Lett. 116, 042903 (2020)
[24] Z. Liang, K. Tang, Q. Shao, G. Li, S. Zeng, and H. Zheng, Synthesis, crystal structure, and photocatalytic activity of a new two-layer Ruddlesden-Popper phase, $Li_2CaTa_2O_7$, Journal of Solid State Chemistry 181, 964 (2008)
[25] B. H. Zhang, Z. Z. Hu, B. H. Chen, X. Q. Liu, and X. M. Chen, Room-temperature ferroelectricity in A-site ordered Ruddlesden-Popper $Li_2CaTa_2O_7$ ceramics, Journal of Materiomics 6, 593 (2020)
[26] S. Kawaguchi, M. Takemoto, K. Osaka, E. Nishibori, C. Moriyoshi, Y. Kubota, Y. Kuroiwa, and K. Sugimoto, High-throughput powder diffraction measurement system consisting of multiple MYTHEN detectors at beamline BL02B2 of SPring-8, Rev. Sci. Instrum. 88, 085111 (2017)
[27] V. Petricek, M. Dusek, and L. Palatinus, Crystallographic Computing System JANA2006:General features, Z. Kristallogr. 229, 345 (2014)
[28] L. Krause, K. Tolborg, T. B. E. Gronbech, K. Sugimoto, B. B. Inverson, and J. Overgaard, Accurate high-resolution single-crystal diffraction data from a Pilatus3 X CdTe detector, *J. Appl. Cryst.* 53, 635 (2020)
[29] G. M, Sheldrick, Crystal structure refinement with SHELXL, Acta Cryst. **C71** (2015) 3-8
[30] P. E. Blöchl, Projector augmented-wave method, Phys. Rev. B: Condens. Matter Mater. Phys. 50, 17953 (1994)
[31] J. P. Perdew, A. Ruzsinszky, G. I. Csonka, O. A. Vydrov, G. E. Scuseria, L. A. Constantin, X. Zhou, K. Burke, Restoring the Density-Gradient Expansion for Exchange in Solids and Surfaces, Phys. Rev. Lett. 100, 136406 (2008)
[32] G. Kresse, and J. Furthmüller, Efficient iterative schemes for ab initio total-energy calculations using a plane-wave basis set, Phys. Rev. B: Condens. Matter Mater. Phys. 54, 11169 (1996)
[33] G. Kresse, D. Joubert, From ultrasoft pseudopotentials to the projector augmented-wave method, Phys. Rev. B: Condens. Matter Mater. Phys. 59, 1758 (1999).
[34] A. Togo, and I. Tanaka, First principles phonon calculations in materials science, Scr. Mater. 108, 1 (2015)
[35] A. Togo, F. Oba, and I. Tanaka, Transition pathway of CO_2 crystals under high pressures, Phys. Rev. B **77**, 184101 (2008)
[36] Y. Mochizuki, T. Nagai, H. shirakuni, A. Nakano, F. Oba, I. Terasaki, and H. Taniguchi, Coexisting Mechanisms for the Ferroelectric Phase Transition in $Li_2SrNb_2O_7$, Chem. Mater, 33, 1257 (2021)
[37] H. Akamatsu, K. Fujita, T. Kuge, A. S. Gupta, A. Togo, S. Lei, F. Xue, G. Stone, J. M. Rondinelli, L. Chen, I. Tanaka, V. Gopalan, and K. Tanaka, Inversion Symmetry Breaking by Oxygen Octahedral Rotations in the Ruddlesden-Popper $NaRTiO_4$ Family, Phys. Rev. Lett. 112, 187602 (2014)
[38] Y. Mochizuki, H. Akamatsu, Y. Kumagai, and F. Oba, Strain-engineered Peierls instability in layered perovskite $La_3Ni_2O_7$ from first principles, Phys. Rev. Materials 2, 125001 (2018)
[39] Y. Mochizuki, Y. Kumagai, H. Akamatsu, and F. Oba, Polar metallic behavior of strained antiperovskites $ACNi_3$(A=Mg,Zn, and Cd) from first principles, Phys. Rev. Materials 2, 125004 (2018)
[40] Y. Mochizuki, H. Sung, A. Takahashi, Y. Kumagai, and F. Oba, Theoretical exploration of mixed-anion antiperovskite semiconductors M_3XN(M=Mg,Ca,Sr,Ba;X=P,As,Sb,Bi), Phys. Rev. Materials 4, 044601 (2020)
[41] R. Dronskowski and P. E. Blöchl, Crystal orbital Hamilton populations (COHP): energy-resolved visualization of chemical bonding in solids based on density-functional calculations, J. Phys. Chem. 97, 8617 (1993)
[42] S Maintz V. L. Deringer, A. L. Tchougreeff, R. Dronskowski, LOBSTER: A tool to extract chemical bonding from plane-wave based DFT, J. Comput. Chem. 37, 1030 (2016)
[43] F. Izumi, and K. Momma, Three-Dimensional Visualization in Powder Diffraction, Solid State Phenom. 130, 15 (2007)
[44] See Supplemental Material at [URL will be inserted by publisher] for the temperature dependent lattice constants and the SHG measurements.
[45] See Supplemental Material at [URL will be inserted by publisher] for the temperature dependent superlattice intensity of LSCNTO-0.5.
[46] See Supplemental Material at [URL will be inserted by publisher] for the temperature dependent superlattice intensity of LSNO.
[47] C. G. alven, D. Mounier, B. Bouchevreau, E.

Suard, A. Bulou, M. Lopez, and F. L. Berre, Phase Transitions in the Ruddlesden-Popper Phase $Li_2CaTa_2O_7$: X-ray and Neutron Powder Thermodiffraction, TEM, Raman, and SHG Experiments, Inorg. Chem. 55, 2309 (2016)

[48] V. M. Ishchuk, V. L. Sobolev, Investigation of two-phase nucleation in paraelectric phase of ferroelectrics with ferroelectric-antiferroelectric-paraelectric triple point, J. Appl. Phys. 92, 2086 (2002)

[49] T. Nagai, Y. Mochizuki, H. Shirakuni, A. Nakano, F. Oba, I. Terasaki, and H. Taniguchi, Phase Transition from Weak Ferroelectricity to Incipient Ferroelectricity in $Li_2Sr(Nb_{1-x}Ta_x)_2O_7$, Chem. Mater. 32, 744 (2020)

[50] J. S. O. Evans, Negative thermal expansion materials, J. Chem. Soc., Dalton Trans 3317 (1999)

[51] We used a space group *Pmcn* for the structural optimization to reduce refinable parameters, although the actual space group of LSCNTO-*x* at 100 K is $P2_1cn$. There are two inequivalent BO_6 octahedral sites in $P2_1cn$, whereas there is only one BO_6 octahedral site in *Pmcn*. In present analyses, we can obtain average δl for the two octahedral sites of LSCNTO-*x* at 100 K by assuming the *Pmcn* structure.

[52] See Supplemental Material at [URL will be inserted by publisher] for the COHPs analysis for LCTO.

[53] See Supplemental Material at [URL will be inserted by publisher] for the crystallographic table for LSNO.

[54] See Supplemental Material at [URL will be inserted by publisher] for the relaxed octahedral geometry of LCTO.

[55] M. I. Aroyo, D. Orobengoa, G. de la Flor, E. S. Tasci, J. M. Perez-Mato and H. Wondratschek, Brillouin-zone database on the Bilbao Crystallographic Server, Acta Cryst. A **70**, 126 (2014)

[56] W. Cochran, Crystal stability and the theory of ferroelectricity, Adv. Phys., 9, 387 (1960)

[57] W. Cochran, Crystal stability and the theory of ferroelectricity part II. Piezoelectric crystals, Adv. Phys., 10, 401 (1961)

[58] J. F. Scott, Soft-mode spectroscopy: Experimental studies of structural phase transitions, Rev. Mod. Phys., 46, 83 (1974)